Article

Unveiling the Synthesis of Strontium Ferrites by Sol-Gel and Laser Floating Zone Methods for Energy Application

Silvia Soreto Teixeira [ID], Rafael Ferreira, João Carvalho [ID] and Nuno M. Ferreira *[ID]

i3N and Department of Physics, University of Aveiro, Campus Universitário de Santiago,
3810-193 Aveiro, Portugal
* Correspondence: nmferreira@ua.pt

Abstract: This work proposes the synthesis of strontium ferrite by two different methods: sol-gel (SG), using powdered coconut water (PCW) as a precursor, and laser floating zone (LFZ). The SG samples were after treated at temperatures of 700, 1000, and 1200 °C, while the samples obtained by LFZ were grown at pulling rates of 10, 50, and 100 mm/h. All samples studied were subjected to structural characterization techniques, as well as electrical (AC and DC) and magnetic characterization. Through X-ray diffraction, it was possible to observe that all the samples presented strontium ferrites, but none were single phase. The phases detected in XRD were confirmed by Raman spectroscopy. Scanning electron micrography allowed the observation of an increase in grain size with the temperature of SG samples and the reduction of the porosity with the decrease in growth rate for LFZ fibers. Through electrical analysis, it was observed that the most suitable samples for energy storage were the samples grown at 100 mm/h ($\varepsilon_r' = 430{,}712$; $\varepsilon_r'' = 11{,}577$; $\tan \delta = 0.84$; $\sigma_{ac} = 0.0006$ S/m, at 1 kHz). The remaining samples had high dielectric losses and can be applied in electromagnetic shielding. The SG 700 °C sample presented the highest magnetization (38.5 emu/g at T = 5 K).

Keywords: energy storage; strontium ferrite; sol-gel method; LFZ method; X-ray diffraction; impedance spectroscopy; dielectric measurements

1. Introduction

Currently, we live in a world that is undergoing an energy revolution. The resources that we have been using and abusing to produce energy are coming to an end, so it is necessary to discover new environmentally friendly materials capable of storing energy. The development of these materials has been growing exponentially because it is in these that the future lies. Ceramic materials capable of storing energy, such as capacitors, have many applications, such as in electric vehicles or electronic devices. The creation of materials with a high dielectric constant and resistance to dielectric breakdown to withstand very high voltages and allow the storage of large amounts of energy [1] is the key to the development of energy stores. For a material to be considered a good energy store, it must have certain characteristics such as low dielectric losses, a high dielectric constant in the case of electrical energy storage and must present, a ferromagnetic behavior with high magnetization in the case of e magnetic energy storage [2].

To protect humans and electronics from hazardous electromagnetic (EM) radiation, electromagnetic shielding can be employed by using certain materials [3]. Two different mechanisms for EM shielding exist. Absorption attenuation and attenuation based on reflection [4]. Materials with high dielectric constants and losses, will provide shielding due to their capability to absorb and dissipate EM radiation.

Ferrites are very interesting materials due to their electrical and magnetic properties, such as high permeability, spontaneous magnetization, low magnetic losses, high electrical resistivity, and high thermal stability, that have been applied in several areas such as high-capacity batteries and in intermediate electrodes in rechargeable batteries [2], due to

these characteristics were selected for this study. Ferrites can crystallize in three different structures: cubic spinel structure (spinel) typical of materials with chemical composition AFe_2O_4 (A = Zn^{2+}, Cu^{2+}, Sr^{2+}, Mg^{2+}), hexagonal structure $A_6Fe_2O_4$ (A = Ba^{2+}, Ca^{2+}, Sr^{2+}) and garnet type structure $3A_2$ $5Fe_2O_6$ (A = Y^{3+}) [5].

Strontium ferrite crystallizes according to a cubic spinel structure (spinel) typical of materials with the chemical composition AB_2X_4 [6]. Each unit cell of the spinel structure is composed of 8 face-centered cubic structures. The X anions, in this case, oxygen (O^{2-}), are arranged in a face-centered cubic structure. The bivalent cation A, in this case strontium, occupies 1/8 of the tetrahedral interstices. The cation B, in this case iron, occupies half of the octahedral interstices [6].

These ferrites have received attention due to their structure, which allows flexibility in the position of metallic cations, as well as the variability of their number of valence electrons, providing the formation of ferrites with different physical properties. Since these are easily modified, they can act as different catalysts, such as photo or electro catalysts, depending on the type of doping performed [7]. It has also drawn attention due to its electromagnetic properties and is currently the subject of many studies of materials development for energy storage. These ferrites present interesting electrical (Table 1) and magnetic properties essential for energy storage, such as high magnetization saturation, high dielectric resistivity, and low electrical losses [8]. These properties are dependent on the preparation method, the chemical composition of the compound, the sintering temperature, the density, and grain size [9,10].

Table 1. Values of electrical properties of different ferrites.

Ferrites	Electrical Properties (@300 K; f = 1 kHz)		
	ε'_r	ε''_r	tan δ
$LiFe_5O_8$ (HT @800 °C) [11]	22.83	2.3	0.1
$Na_3Fe_5O_9$ (HT @1100 °C) [12]	807.8	285.1	0.35
$Y_3Fe_5O_{12}$ (HT @1000 °C) [13]	11.49	1.15	0.1
$SrFe_6O_{13}$ (HT @1100 °C) [14]	5.5	10^{-1}	0.01
$SrFe_{12}O_{19}$ (HT @650 °C) [15]	12	7	0.6
$NiFe_2O_4$ (HT @1100 °C) [16]	5	7	0.6

The sol-gel method has been widely used for the formation of nanometric particles. This process consists of the formation of a colloidal solution (called sol), which subsequently passes to a gelation phase through a thermal treatment to form a three-dimensional network. Powdered coconut water (protein route) has been used as a chelating agent, which allows the metallic ions to be fixed in the solution, forming a soluble and non-toxic complex [1]. This process makes it possible to obtain the desired crystalline phase using relatively low temperatures, which facilitates its manufacture at a low production cost, with the advantage of obtaining nano-sized particles with low contamination [17] and excellent chemical homogeneity, on the other hand, some of the disadvantages of this process are the loss of a lot of organic material [1]. The passage of the solution from the sol phase to the gel phase is accompanied by a change in the pH of the solution. The pH variation causes variations in the structural and magnetic properties of the nanoparticles; that is, with the increase in the basicity of the solution, the forbidden energy band decreases, as well as the magnetization value [18].

There are several preparation SG methods, but the most used is the Pechini route, which consists of using citric acid to form chelates with metallic cations, used to form a polymeric network with the aid of ethylene glycol. This solution is subsequently heated, initiating the esterification process between citric acid and ethylene glycol resulting in the formation of a ceramic material [19].

The laser floating zone (LFZ) method allows the growth of materials with a very high melting temperature due to the focus of a CO_2 laser on materials that absorb this wavelength. This method provides the growth of a material with a crystallographic alignment [20]. The formation of ferrites takes place inside a growth chamber that can work at different atmospheres and pressures, which interact with the kinetic of the crystallization process. Inside the growth chamber, a system of mirrors is responsible for focusing the laser light on the sample. To control the growing process, a homemade program is used to control the power laser and pulling rate (growth rate) and allows us, to observe the melted region in real-time. The growth rate parameter is extremely important in the crystallization process. A slower growth rate provides the growth of larger crystals with a more homogeneous composition and normally without secondary phases, but this also depends on the material and phase stability, in contrast to the higher growth rate [21].

The focus of this study was the energy storage capacity of strontium ferrites, namely $SrFe_2O_4$, obtained by two different preparation methods, the sol-gel (SG) method, where nitrates were used as base materials for the formation of strontium ferrite and the laser floating zone (LFZ) method where the ferrites were formed based on oxides. The use of two different methods allows a comparison to define the most efficient method and the one that produces a better material for energy storage. The samples obtained were analyzed using several techniques, allowing their microstructural, morphological, electrical, and magnetic characterization as energy storage material.

2. Materials and Methods

2.1. Preparation by Sol-Gel via Protein

Strontium ferrite ($SrFe_2O_4$) was made by sol-gel (SG) technique, the formation of ferrite is carried out from nonahydrate iron nitrate [$Fe(NO_3)_3 \cdot 9H_2O$, Aldrich- Darmstadt, Germany, 99.8%] and strontium nitrate [$Sr(NO_3)_2$, Aldrich- Darmstadt, Germany, 99.8%]. The aim is to form strontium ferrite ($SrFe_2O_4$), starting from metallic nitrates, considering the stoichiometry of the chemical reaction, 2 mol $Fe(NO_3)_3 \cdot 9H_2O$: 1 mol $Sr(NO_3)_2$. A coconut water solution is used as a chelator, in addition to the fact that it is rich in proteins that are responsible for binding to metal ions forming the polymeric network, hence the name of this route as a protein pathway [22]. Powdered coconut water (PCW), a precursor of the reaction, was used in excess in a stoichiometry of 2 mol (PCW): 1 mol ($SrFe_2O_4$) to guarantee that the intended reaction occurred. The coconut water solution, after being prepared, was added to the mixture of nitrates. After homogenizing the mixture, a first pH measurement was performed at room temperature (20 °C), obtaining an initial value of 1.4. For the formation of the gel, the solution was mixed with the aid of a magnetic stirrer on a heating plate. Initially, the solution was placed at a temperature of 80 °C for two hours, during which time the pH of 30 was measured every 30 min. Subsequently, the temperature was raised to 100 °C for two hours, and the pH was measured every half hour.

Despite the oscillation of the pH values, it is possible to verify that initially, the pH value decreased slightly, and after 90 min, a variation of this tendency occurred with an increase, obtaining the final value of 1.60 after 255 min. It is assumed that when the trend inversion of the pH value occurs, the intended chemical reaction occurs, that is, the formation of the gel. With the change in the pH value, it was possible to verify that both the color and the consistency of the solution began to change, changing from a very aqueous solution with a dark brown color to a thick and clearer solution. Finally, the gel was obtained and was taken to the oven to remove excess solvent. During the first 30 min, the temperature was increased to 350 °C with an increment of 10 °C per minute. Once 350 °C was reached, this temperature was maintained for 1 h. Then, the oven was cooled down through its thermal inertia.

The solution was then ground to obtain a powder that was used to create the pellets, which were later treated and analyzed. Each pellet was made with approximately 180 mg of powder and with the addition of a drop of polyvinyl alcohol (PVA, Merck-Darmstadt, Germany, 99%), enabling the bonding of the nanoparticles. After being well mixed, the final

product was placed in a steel mold with a diameter of 13 mm, and a pressure of 3 tons/cm^2 was applied using a uniaxial hydraulic press.

After compression of the powder, the pellets were thermally treated. This thermal treatment has as its main objectives the formation of the intended crystalline phase as well as the densifying of the pellets, through a sintering process. Sintering provides a reduction in the pores of the pellets due to the increase in the grain and increases their resistance to external forces (mechanical resistance) [1,23].

The heat treatments all started with an increase in temperature at a rate of 5 °C/min until 100 °C was reached. Once this level was reached, it was maintained for one hour to remove humidity present in the pellet. Subsequently, the temperature was increased at the same rate until the desired temperature was reached, according to the analysis of the results obtained in the differential thermal analysis (DTA) and thermogravimetric analysis (TGA).

2.2. Preparation by Laser Floating Zone

This preparation technique aims to create rods of strontium ferrite that will later be used as seeds and feed for the growth of the fiber. The formation of this material is achieved with a laser beam to melt the precursor and initiate the crystallization process. This system is controlled and monitored, allowing the fiber growth process to be carried out according to a specific growth rate.

The formation of the strontium fiber obtained by this method is based on iron oxide (Fe_2O_3, Aldrich- Darmstadt, Germany, 99.8%) and strontium carbonate ($SrCO_3$, Aldrich-Darmstadt, Germany, 99%), which were used to obtain the following stoichiometry: $SrFe_2O_4$.

After weighing the reagents, the powders were placed in an agate vessel together with spheres of various sizes and alcohol as a dispersing medium. The Agata vessels were placed in the planetary mill for 2 h with a rotation speed of 250 rpm. This process allowed the formation of a homogeneous powder resulting from the mixture of iron oxide and strontium carbonate.

After mixing the powders, a mixture of polyvinyl alcohol (PVA, Merck-Darmstadt, Germany, 99%) and distilled water at a concentration of 0.1 g/mL was added to facilitate the binding of the particles, creating a more consistent mixture. Then, the mixture was cold extruded, creating rods with a circular base of 3 mm and lengths up to 12 cm, which had a clay-like texture. After drying at room temperature, in a mold so that they were as straight as possible, the dried fibers were then placed in the LFZ system, equipped with a Spectron SLC 200 W CO_2 laser of 200 W with a wavelength of 10.6 μm.

Fibers were grown at 10, 50 and 100 mm/h, with constant laser power at room conditions. This power was defined so that the melting process presents as consistent and homogeneous as possible. The growth rates were chosen to observe their effect on the electrical and magnetic material properties.

The feed rotates at 15 rpm while the seed at −5 rpm (in the opposite direction to the rotation of the seed), obtaining a fiber as shown in Figure 1. At the base, a reddish color can be observed corresponding to the initial phase before growth (raw material). The dark grey area corresponds to the beginning of the growth process, and the metallic area to a fully formed fiber.

2.3. Characterization Techniques

The differential thermal and thermogravimetric analyses of the ferrites produced by the sol-gel method were carried out in the Hitachi (Tokyo, Japan) STA7300 equipment, from a temperature of 40 °C to 1200 °C, with a heating rate of 5 °C/min, in a nitrogen atmosphere (50 mL flow rate). This technique was not performed on LFZ samples, since in these the heat treatments were not necessary.
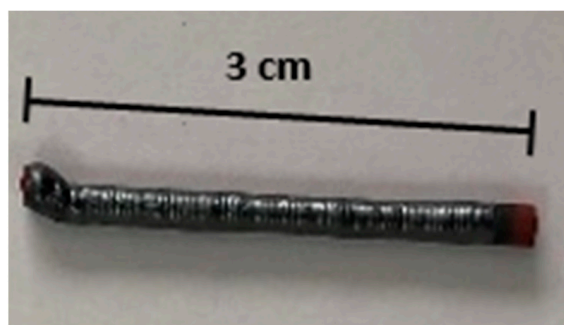
Figure 1. Example of strontium ferrite fiber produced by the LFZ method.

X-ray diffraction powder analysis (XRD) was made using Malvern Panalytical (Malvern, UK) AERIS equipment with a CuK α radiation, a wavelength of 1.54060 Å at 40 kV and 15 mA, with a 2θ angle step of 0.0220°. The peaks were indexed using the ICDD (International Central for Diffraction Data) database.

Scanning electron microscopy (SEM) is a technique that allows knowing the morphology, composition, and orientation of the grains of the sample material under study [24]. A Tescan (Brno, Czechia) Vega 3 microscope with a Brunker (Billerica, MA, USA) X-ray detector was used. For sample analysis, a layer of carbon was deposited. The samples obtained through the LFZ method were impregnated in resin and subsequently polished up to 1 μm polishing cloths.

Raman spectroscopy is a technique used to identify and quantify the compounds present in the sample and to obtain physical characteristics through the vibration of molecules [25,26]. A Jobin-Yvon (Palaiseau, France) HR-800-UV spectrometer was used at room temperature with a laser with a wavelength of 532 nm (green), using a magnification of 50 times.

For DC voltage, the samples were prepared by placing silver paste on both circular surfaces of the sample together with two conductive wires. These data were used to plot the graph of electrical conductivity as a function of time at room temperature. A Keithley model 617 electrometer was used for this analysis.

For carrying out the AC electrical measurements, the samples obtained by the sol-gel method already had an ideal geometry (sample thickness much smaller than its diameter) using the parallel plate condenser model. On the other hand, the samples obtained by LFZ had an opposite geometry, so it was necessary to carry out several treatments/polishing to obtain a sample with the necessary characteristics. Agilent (Santa Clara, CA, USA) 4294 impedance analyzer was used to carry out AC measurements. The measurements were carried out with a sinusoidal voltage of 0.5 V and a frequency range from 100 Hz to 1 MHz at room temperature.

The magnetic behavior of the samples was measured for all samples between 5 and 300 K, recording the magnetization value as a function of temperature (Field Cooled and Zero Field Cooled, at H = 0.1 T) and magnetic field (hysteresis measurements between ±10 T).

3. Results and Discussion

The powder obtained by the sol-gel method was submitted to thermal analysis, to perform a thermal characterization, where it was possible to identify possible transformations that occur in the sample, with the temperature increases, allowing us to define adequate treatment temperatures. The curves obtained in the DTA and TGA analyses, are shown in Figure 2.
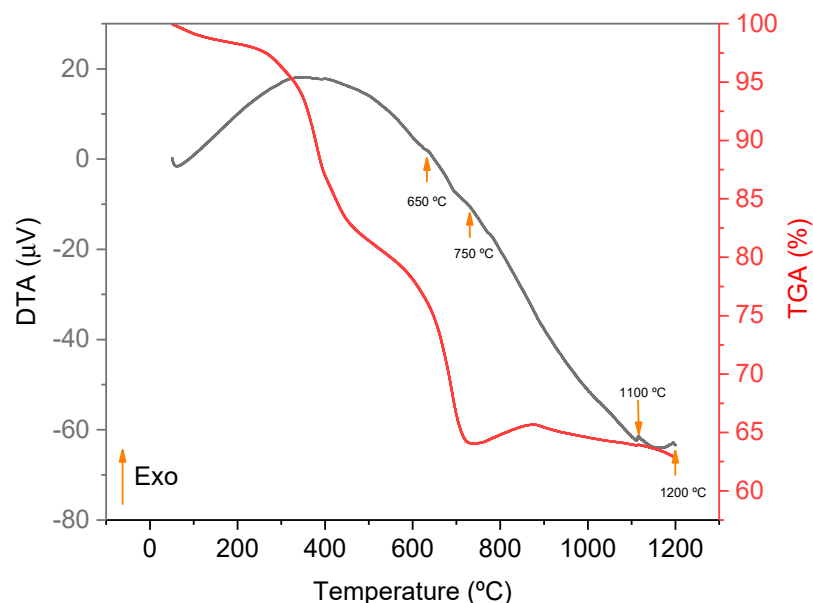
Figure 2. Graphs obtained in the DTA and TGA analyses of the powders obtained by sol-gel.

Figure 2 shows three distinct regions of mass loss. The first region is found between 50 and 400 °C, where a loss of 15% occurs due to the nitrate's elimination present in the sample [27]. A second region from 400 to 700 °C, where a possible mass loss of 20% is observed due to the evaporation of organics [28], accompanied by an exothermic peak in the DTA curve, which may be associated with the formation of a crystalline phase, at a temperature of approximately 650 °C. Between 750 and 850 °C there is a mass gain of 3% followed by a new exothermic peak at 750 °C. Finally, between 900 and 1200 °C, there is a new mass loss of 2%. In this region, it is also possible to observe two exothermic peaks, one at 1100 °C and another at 1200 °C, which most likely occur due to the formation of new crystalline phases.

Considering results obtained from DTA curves, temperatures of 700, 1000 and 1200 °C were chosen for the thermal treatments of the samples produced by the sol-gel method since, according to the results of the thermal measurements, at these temperatures important chemical and structural transformations take place.

After heat-treating the powders obtained by sol-gel at temperatures of 700 °C, 1000 °C, and 1200 °C, X-ray diffractograms were obtained (Figure 3a–c, respectively). Analyzing the results obtained for the sol-gel samples at a temperature of 700 °C, the phases $SrFe_2O_4$, $SrFeO_3$, and Fe_2O_3 were detected. Increasing the temperature, the samples underwent several changes, observing different crystalline phases for the samples treated at 1000 and 1200 °C, which can be attributed to $Sr_4Fe_6O_{13}$ and $SrFe_{12}O_{19}$. According to the literature, these two phases were found at a temperature of 1100 °C [14,29]. It is possible to observe that with temperature increases, the strontium ferrite phase ($SrFe_2O_{4)}$ begins to transform into other phases. This transformation is gradual, and therefore, the appearance of new phases should begin shortly after the temperature of 700 °C, most likely related to the exothermic peaks at temperatures of 750, 1100, and 1200 °C, as shown in Figure 2.

The diffractograms of the samples obtained by LFZ at the rates of 10, 50, and 100 mm/h (Figure 3d–f, respectively) were not possible to associate with a single phase. These samples show two phases, associated with $Sr_4Fe_6O_{13}$ and $SrFe_{12}O_{19}$, also present in the sol-gel samples heat treated at 1000 and 1200 °C. In the LFZ, since all samples are obtained through melting, the temperature is not a variable that can be changed. However, the growth rate is a factor that controls the formation of new phases.
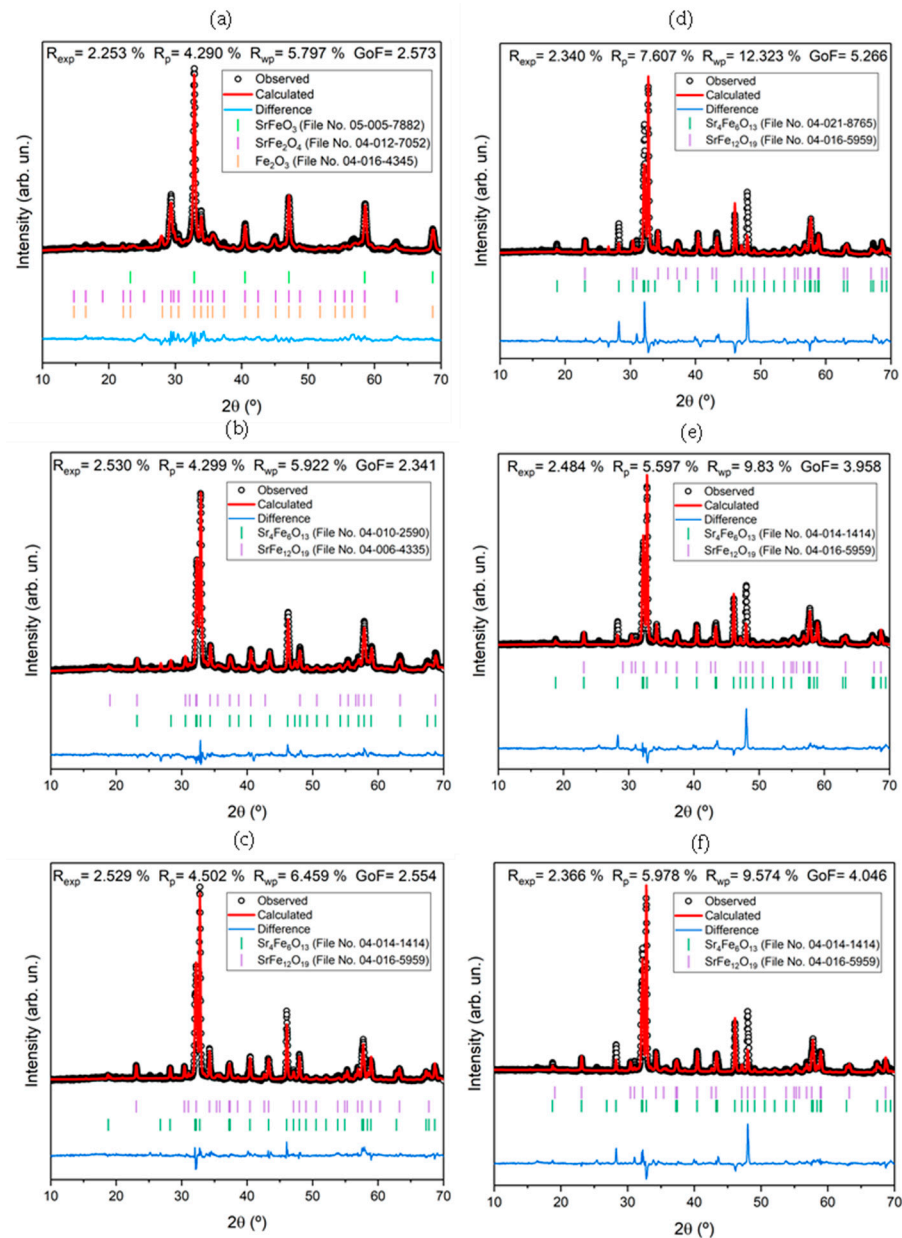
Figure 3. X-ray diffractograms and the Rietveld fitted curves for samples (**a**) SG 700 °C, (**b**) SG 1000 °C, (**c**) SG 1200 °C, (**d**) LFZ 10 mm/h, (**e**) LFZ 50 mm/h and (**f**) LFZ 100 mm/h.

Rietveld refinements were performed on all diffractograms obtained (Figure 3). The SG samples present a good fit based on the Goodness of Fit (GoF) parameter. For the LFZ samples, the GoF is higher, mainly due to the peaks around the 28 and 48° marks. The high intensity of these peaks makes the GoF higher due to the bad fit, which can be owed to the fact that the LFZ samples can present a reduction of oxygen atoms, influencing the intensity and the shift of peaks [30].

From the Rietveld refinements, quantitative analysis was also performed, and is presented in Table 2. For the sol-gel samples, it is possible to verify that the desired phase of $SrFe_2O_4$ is present in the sample heat-treated at 700 °C, with a percentage of 38.3%. Between the samples heat treated at 1000 and 1200 °C, a slight increase in the $SrFe_{12}O_{19}$ composition is observed, with the increase in heat treatment temperature. This is corroborated by the results obtained for the LFZ samples, where the increase in pulling rate and a decrease in temperature in the fiber leads to a decrease in the $SrFe_{12}O_{19}$ phase.

Table 2. Composition percentages obtained from Rietveld refinements for all the synthesized samples.

Sample	Composition
SG 700 °C	$SrFeO_3$ (47.2%) $SrFe_2O_4$ (38.3%) γ-Fe_2O_3 (14.5%)
SG 1000 °C	$Sr_4Fe_6O_{13}$ (78.2%) $SrFe_{12}O_{19}$ (21.8%)
SG 1200 °C	$Sr_4Fe_6O_{13}$ (76.5%) $SrFe_{12}O_{19}$ (23.5%)
LFZ 10 mm/h	$Sr_4Fe_6O_{13}$ (76.5%) $SrFe_{12}O_{19}$ (23.5%)
LFZ 50 mm/h	$Sr_4Fe_6O_{13}$ (78.2%) $SrFe_{12}O_{19}$ (21.8%)
LFZ 100 mm/h	$Sr_4Fe_6O_{13}$ (79.1%) $SrFe_{12}O_{19}$ (20.9%)

The Raman spectra (Figure 4a,b) show the existence of a vibration mode at 700 cm^{-1}. This mode is visible in all samples except the sample obtained by the SG method at 700 °C, corroborating the XRD results showing that this sample presents different phases when compared to the other samples. According to the literature [31,32], this vibrational mode at 700 cm^{-1} is related to the existence of strontium hexaferrite ($SrFe_{12}O_{19}$), which is precisely found in samples that present this mode of vibration. Another evident mode is found between 1250 and 1500 cm^{-1}, which, according to the literature, corresponds to the formation of hematite (Fe_2O_3) [33]. The existence of vibration bands at 213, 285, 301, and 402 cm^{-1} are also noticeable, which, according to the literature, are associated with the presence of the α-Fe_2O_3 phase [34]. This crystalline phase is not present in the samples according to the X-ray diffraction analysis; this fact is attributed to its crystallinity not being sufficient to be detected.

(**a**) SG Samples   (**b**) LFZ samples
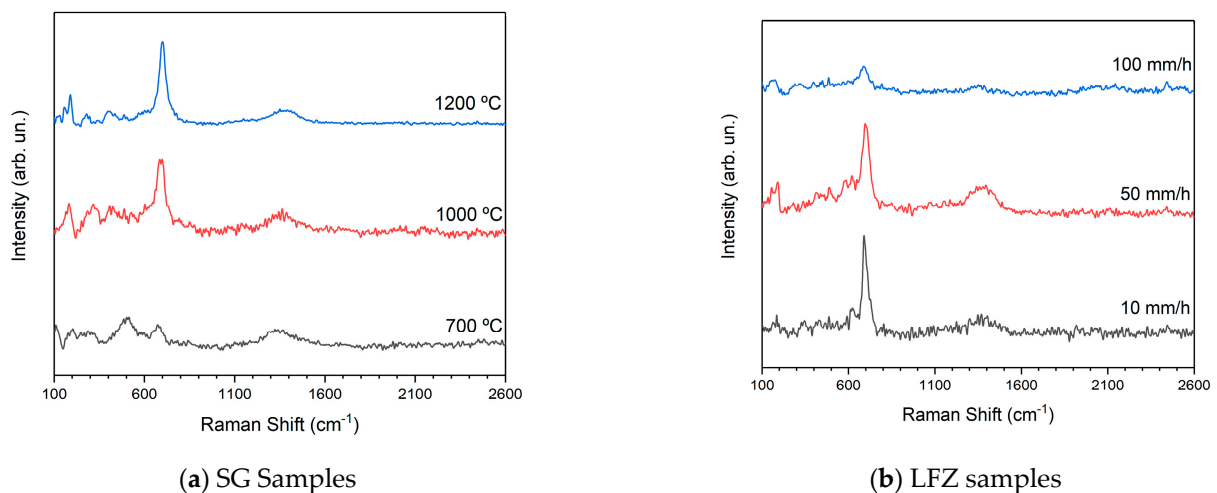
Figure 4. Raman spectra for (**a**) samples obtained by LFZ and (**b**) sol-gel samples.

From Table 3, it is possible to observe that with the increase in treatment temperature, the grain size increases, and the samples become less porous, showing a similar behavior to those reported in the literature [1]. In the sample treated at 700 °C, the grains that make up the sample are all the same, producing a very uniform surface with agglomerated grains, as described in the literature [35]. As the temperature of the heat treatment increases, grains with different shapes and sizes begin to appear. In the sample treated at 1000 °C, it is possible to observe the appearance of grains with different shapes (within the circumfer-

ences in the image), some with a pointed shape, others with a round shape, and it is also possible to observe grains that are very similar to the grain present in the sample treated at 700 °C. In the sample treated at 1200 °C, these grains are no longer so visible, probably due to coalescence related to the heat treatment temperature. The change in the shape and size of grains between the SG 700 °C and 1200 °C can be seen as the appearance of new phases of strontium ferrite, which has already been shown both in XRD analysis and by Raman spectroscopy. All samples, according to the EDS map (Table 3), are formed only by strontium, iron, and oxygen, which is also corroborated by the previously mentioned analysis methods.
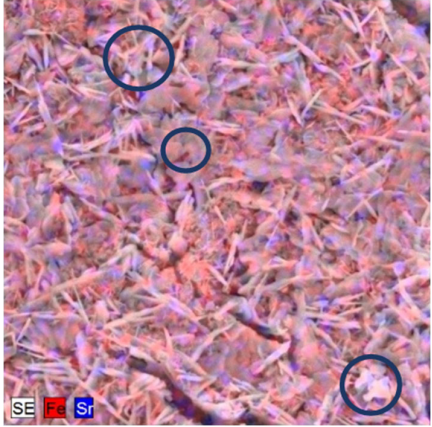
Table 3. Micrographs and EDS maps for heat-treated SG samples.
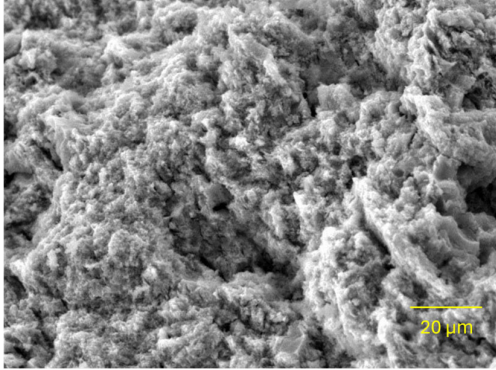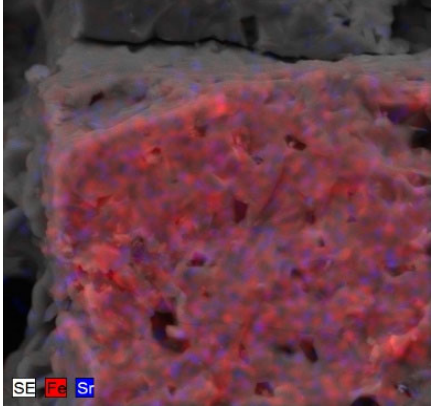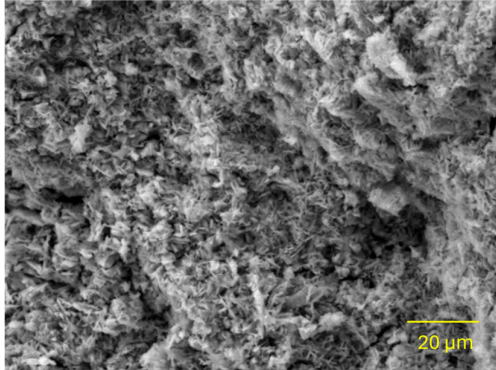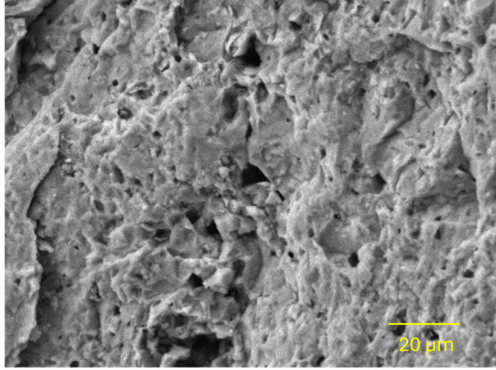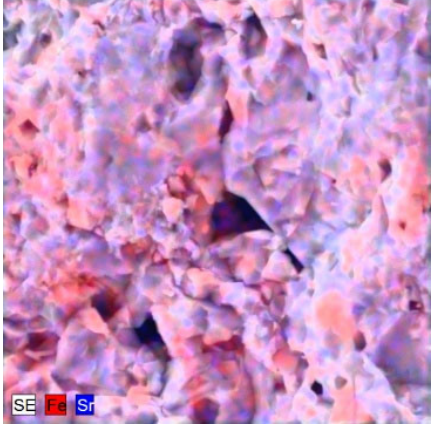
Sample	Micrograph	EDS Map
700 °C		
1000 °C		
1200 °C		

Table 4 presents the micrographs of the polished longitudinal surfaces of the samples obtained by the LFZ method. It is possible to observe in all samples, the orientation of the phases (vertical) and the formation of zones that predominantly contain iron (red in the EDS map) and other regions with strontium and iron (blue in the EDS map), confirming the results from XRD and Raman analyses. From the EDS analysis, it was possible to verify the distribution of the majority of elements on the surface of the samples of iron (52.5%) and strontium (47.5%) related to the major phase $Sr_4Fe_6O_{13}$. Regions with different ratios of iron and strontium were also observed related to the phase $SrFe_{12}O_{19}$. In the sample grown at 10 mm/h, it is possible to observe that the crystals align with the growth direction. In the sample obtained with a growth rate of 100 mm/h, crystals parallel to the growth of the fiber are visible. These crystals are very long, almost the length of the fiber, and regular. In the sample with a growth rate of 50 mm/h, the crystals are not as regular, have a greater width, and are not all oriented in the direction of growth. This behavior agrees in line with the literature [36].

Comparing the micrographs from both methods (Tables 3 and 4), it is possible to observe that the LFZ provides the formation of samples with a much smaller grain boundary density. This difference was expected to influence the electrical conductivity of the samples [37]. Moreover, by analyzing the distribution of elements in the EDS map (Table 4), it was possible to confirm the existence of at least two regions/phases in the sample grown at 50 mm/h. One of them has a ratio of Sr/Fe, which may be related to the $Sr_4Fe_6O_{13}$ phase detected through XRD analysis. The other phase found has a higher ratio of Fe than Sr, confirming the $SrFe_{12}O_{19}$ phase detected by XRD (Figure 3).

Table 4. Micrographs and EDS maps obtained for samples grown by LFZ.

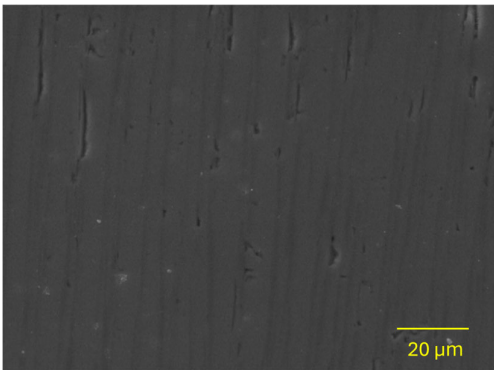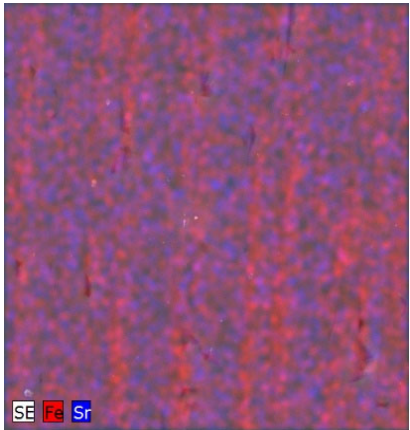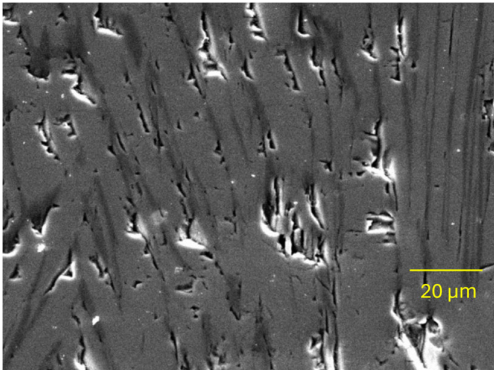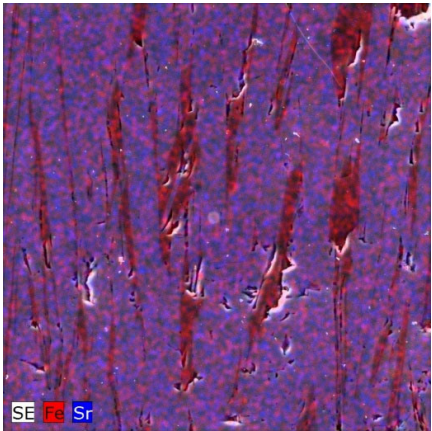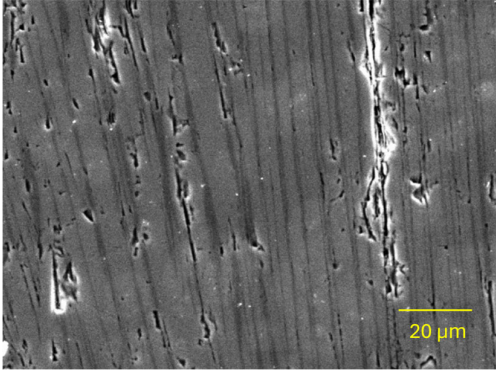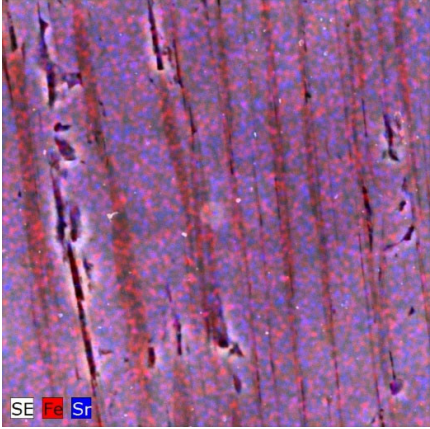| Samples	Micrography	EDS Map
10 mm/h		
50 mm/h		

Table 4. *Cont.*

Samples	Micrography	EDS Map
100 mm/h		

The DC conductivity measurements (Figure 5a) at 300 K show that thermal treatments at higher temperatures result in higher conductivity. This may be related to the grain size that increases with the increase in temperature due to the sample becoming less porous, increasing electrical conduction. According to the literature [38], this phenomenon of increased conductivity with increasing grain size is common; nevertheless, after a certain grain size, this trend reverses.
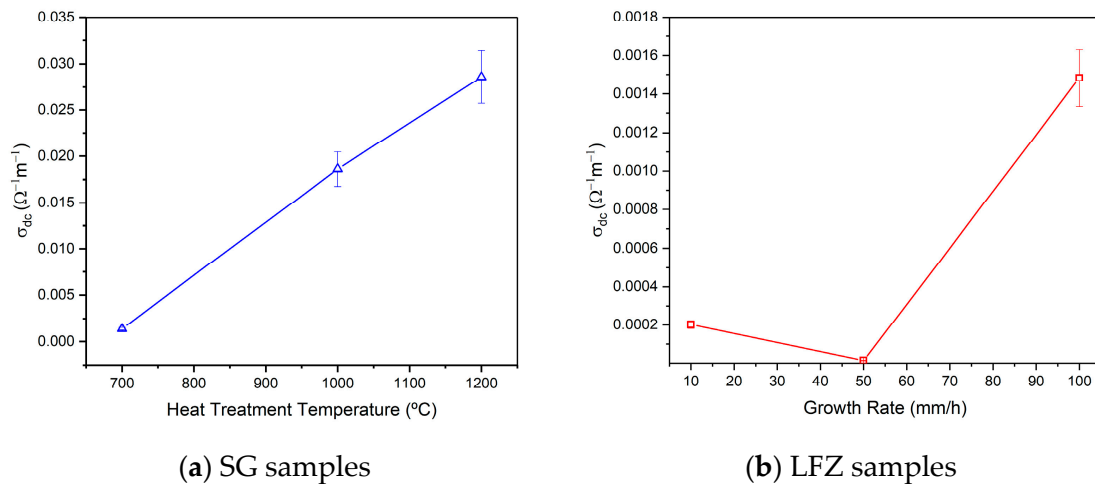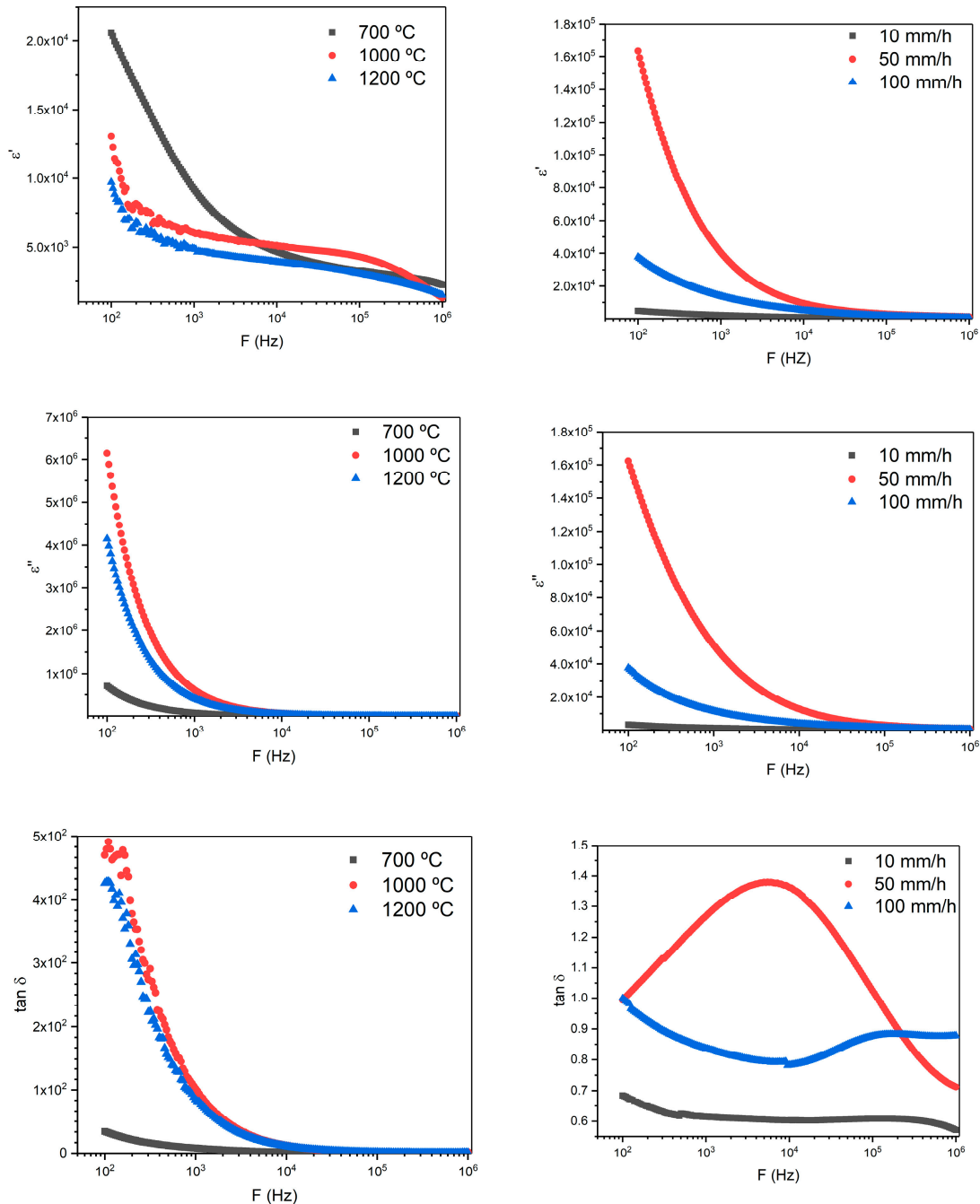

(a) SG samples

(b) LFZ samples

Figure 5. DC conductivity at 300 K values for samples obtained by (**a**) SG and (**b**) LFZ methods.

For the samples obtained with LFZ (Figure 5b), the variation of the conductivity values is not linear with the increase/decrease in the fiber growth velocity. The fiber grown at a rate of 50 mm/h is the one with the lowest DC electrical conductivity, followed by the 10 mm/h fiber and finally the 100 mm/h fiber. These results can be attributed to the higher porosity of the sample grown at 50 mm/h.

Comparing the results of the samples obtained, it is possible to verify that the sample with the highest DC conductivity is the sample obtained by SG treated at 1200 °C, with a value of σ_{dc} = 0.030 S/m, which is much higher than the maximum conductivity value obtained by LFZ, which was the sample grown at a rate of 100 mm/h with a value of σ_{dc} = 0.0016 S/m.

Analyzing the graphs of dielectric constant (ε_r') and dielectric losses (ε_r'') at 300 K (Figure 6), it is possible to confirm that both magnitudes decrease with increasing frequency. This trend is common to all samples obtained by SG (Figure 6a) and by LFZ (Figure 6b).

The dielectric constant decreases with increasing frequency because the polarization of dipoles, present in ferrite, decreases at higher frequencies. Dielectric losses may increase with frequency and then decrease, resulting in a process of dielectric relaxation. Based on the literature [35,39], this behavior is common to ferrites since, from a certain frequency, the exchange of electrons cannot follow the variation of the applied electric field; that is, the polarization of the material cannot follow the direction in which the field it is applied, resulting in a decrease in the ε_r' [35,39].

(**a**) SG samples   (**b**) LFZ samples

Figure 6. Dielectric measurements as a function of frequency, at 300 K, for (**a**) SG and (**b**) LFZ samples.

According to the literature [35], with the increase in the treatment temperature, an increase in the dielectric constant and dielectric losses occurs [35], and this behavior is also

observed in other ferrites. This phenomenon was not verified in the analyzed samples (Figure 6a,b). In our work, in the case of the dielectric constant, the opposite was observed since, for a frequency of 1 kHz, the sample that presents the highest dielectric constant is the sample treated at lower temperature (700 °C, $\varepsilon_r' = 9219$) decreasing up to sample treated at high temperature (1200 °C, $\varepsilon_r' = 4899$). This phenomenon may be related to the crystalline composition of the samples since, according to the X-ray analysis, the sample treated at 700 °C presents a single phase of $SrFe_2O_4$, and the other two samples heat treated have several crystalline phases with similar compositions. Another important variable for this behavior obtained is the different grain size since the sample treated at 700 °C has a smaller grain size than the other samples treated at high temperatures. This implies that there are more grain boundaries, which leads to an increase in the polarization between the contacting faces of the grains, thus increasing the dielectric constant [40], known as Maxwell-Wagner-Sillars polarization. In terms of dielectric losses, the one with the highest losses for 1 kHz is the sample treated at 1000 °C ($\varepsilon_r'' = 615,613$), and the one with the lowest losses is the sample treated at 700 °C ($\varepsilon_r'' = 75,152$). Once again, the behavior of the samples treated at 1000 and 1200 °C have very similar behavior, with the sample treated at 700 °C showing the greatest difference in the values obtained. This result is due to the crystalline composition of the samples, as well as the size and shape of the grain of the samples, confirmed by SEM analysis.

Analyzing the graphs obtained for the LFZ samples (Figure 6b), it was possible to observe a dielectric constant increase with the decrease in the growth rate of the LFZ samples. Comparing the results obtained from the LFZ samples with the SG samples and considering the X-ray analysis, it was possible to verify that the samples obtained by LFZ with a lower growth rate have a phase composition like samples heat treated at higher temperatures. Therefore, it is expected that the sample with the highest growth rate will have the highest dielectric constant, as well as the sample treated at the lowest temperature.

For 1 kHz and 300 K, the dielectric constant has values of $\varepsilon_r' = 2217$ for the sample grown at 10 mm/h, $\varepsilon_r' = 40,485$ for 50 mm/h, and $\varepsilon_r' = 430,712$. However, in dielectric losses, this connection is not verified since the sample that presents greater losses is the sample growth at 50 mm/h ($\varepsilon_r'' = 51,336$), and the one with smaller losses is the sample grown at 10 mm/h ($\varepsilon_r'' = 1363$). This may be related to the low density of grain boundaries, discussed in the analysis of the micrographs of the LFZ samples.

Comparing the values obtained for all samples, it is possible to verify that, at a frequency of 1 kHz, all LFZ samples present lower dielectric losses than the SG samples. As for the dielectric constant, the sample grown at 10 mm/h has a lower value than all LFZ samples at a frequency of 1 kHz. On the other hand, the LFZ samples have dielectric constants four times higher than the samples obtained by SG. According to the literature [39,41], it is common for dielectric losses to decrease with increasing frequency. In sol-gel samples, the decreasing trend of dielectric losses with increasing frequency is clear and happens for all samples. Analyzing Figure 6a, it is possible to observe that the samples treated at 1000 and 1200 °C have present tan δ very similar for the entire range of frequencies, which was to be expected once, according to the X-ray analysis, their crystalline composition is very similar. The sample treated at 700 °C presents the lowest values for the dielectric loss tangent.

The samples obtained by LFZ (Figure 6b) do not show such a coherent behavior. The sample grown at 10 mm/h is the only one that follows the pattern, where the value tan δ decreases with frequency increases. For the sample obtained at 100 mm/h, a peak is observed at higher frequencies, suggesting a relaxation process. The sample grown at 50 mm/h exhibits very different behavior, as its tan δ increases up to the frequency of 5 kHz and then starts to decrease.

Analyzing the values obtained for the frequency of 1 kHz, all the samples obtained by LFZ have lower values of tan δ, with the sample grown at 10 mm/h presenting the lowest value (tan δ = 0.61) while the sample treated at 700 °C presents the lowest value for SG samples, with a value of tan δ = 8.40.

Conductivity AC increases with increasing frequency in all samples (Figure 7) at a temperature of 300 K, which is in line with the literature [35,42,43]. Conductivity is related to the number of charge carriers that respond to changes in frequency and temperature [43]. At low frequencies, AC conductivity is affected by grain boundaries, on the other hand at high frequencies, grain boundaries are a catalyst for AC conductivity [42].
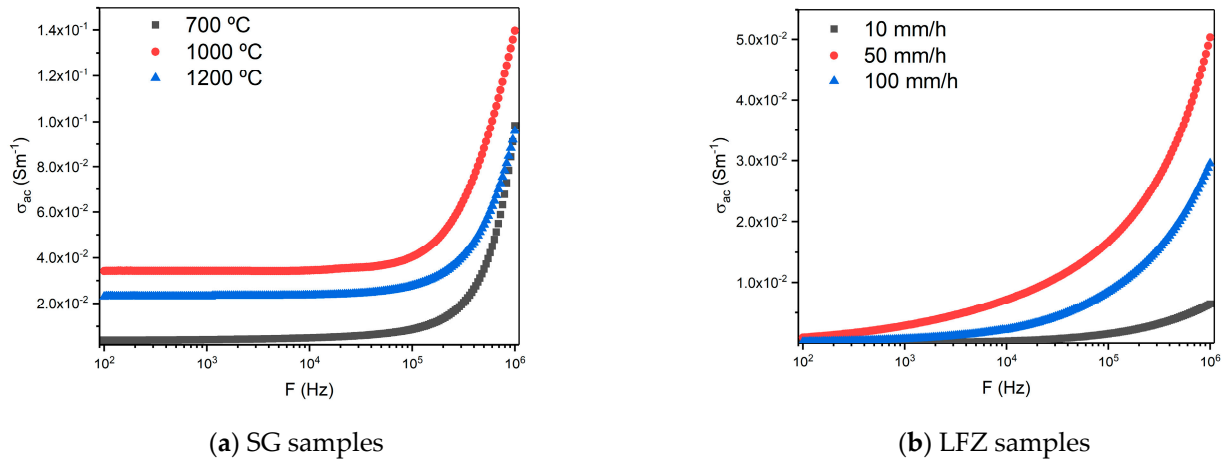

(**a**) SG samples

(**b**) LFZ samples

Figure 7. AC conductivity as a function of frequency at 300 K for (**a**) SG and (**b**) LFZ samples.

The samples formed by SG (Figure 7a), all present a very similar behavior, initially the conductivity has a practically constant value, but from a frequency of 10 kHz the conductivity value starts to increase exponentially. In the frequency range analyzed, the sample treated at 1000 °C is the one with highest conductivity and the sample treated at 700 °C with the lowest conductivity.

The samples obtained by LFZ (Figure 7b), show from low to high frequencies, an increase in conductivity. In all the frequency range the sample that has more AC conductivity is the sample grown at 50 mm/h and the sample that presents less conductivity is the 10 mm/h.

For 1 kHz, the sample with the lowest AC conductivity is the sample grown at 10 mm/h with a conductivity of $\sigma_{ac} = 7.5 \times 10^{-5}$ S/m, the one with the lowest value is the sample treated at 1200 °C with a value of $\sigma_{ac} = 2.0 \times 10^{-2}$ S/m. In general, all samples obtained by LFZ have lower AC conductivity than samples obtained by SG, which is expected since the latter exhibit lower dielectric losses (ε_r'').

Analyzing the results in general and considering a material to be good for energy storage, it needs to present a high dielectric constant and low losses. It is possible to conclude that of the samples obtained by SG, the most appropriate would be the sample treated at 700 °C. In the samples obtained by LFZ, there is none that truly stands out. However, the most appropriate seems to be the sample grown at 100 mm/h since it has a higher dielectric constant and relatively low losses. Comparing these two samples (700 °C and 100 mm/h), the most appropriate for energy storage would be the sample obtained by LFZ, grown at 100 mm/h, since it presents higher values of dielectric constant and lower losses. Yet, all the samples have high electrical dielectric constant; they also have very high dielectric losses, so their use for energy storage is not suitable. Nevertheless, the remaining samples, since they present very high dielectric losses, could be applied in electromagnetic shielding devices.

Concerning the magnetic studies, analyzing the hysteresis cycles obtained for the SG samples (Figure 8a), as expected, it is possible to verify that the samples subjected to a magnetic field at a temperature of 5 K have greater magnetization for H = 5 T than the samples analyzed at 300 K. The sample treated at 700 °C is the one with the highest magnetization: 38.6 emu/g at 5 K and 24.6 emu/g at 300 K. This high magnetization can be due to the γ-Fe$_2$O$_3$ phase, existent in the sample, as this phase, according to literature, can

present a 74 emu/g saturation magnetization at 300 K [44]. The $SrFeO_3$ sample presents a negligible magnetization, while the $SrFe_2O_4$ can present a saturation magnetization of around 12 emu/g at ambient temperature. For the samples treated at 1000 and 1200 °C, despite the former presenting a higher hysteresis, the saturation magnetization practically does not vary from one sample to the other. This phenomenon may be related to the crystalline composition of the samples since, according to X-ray diffraction, these are very similar in the crystalline phases. Although these samples also present in their composition a high magnetization phase, $SrFe_{12}O_{19}$, with a saturation magnetization upwards of 70 emu/g [45], their bigger grain size can lower the magnetization of the samples.
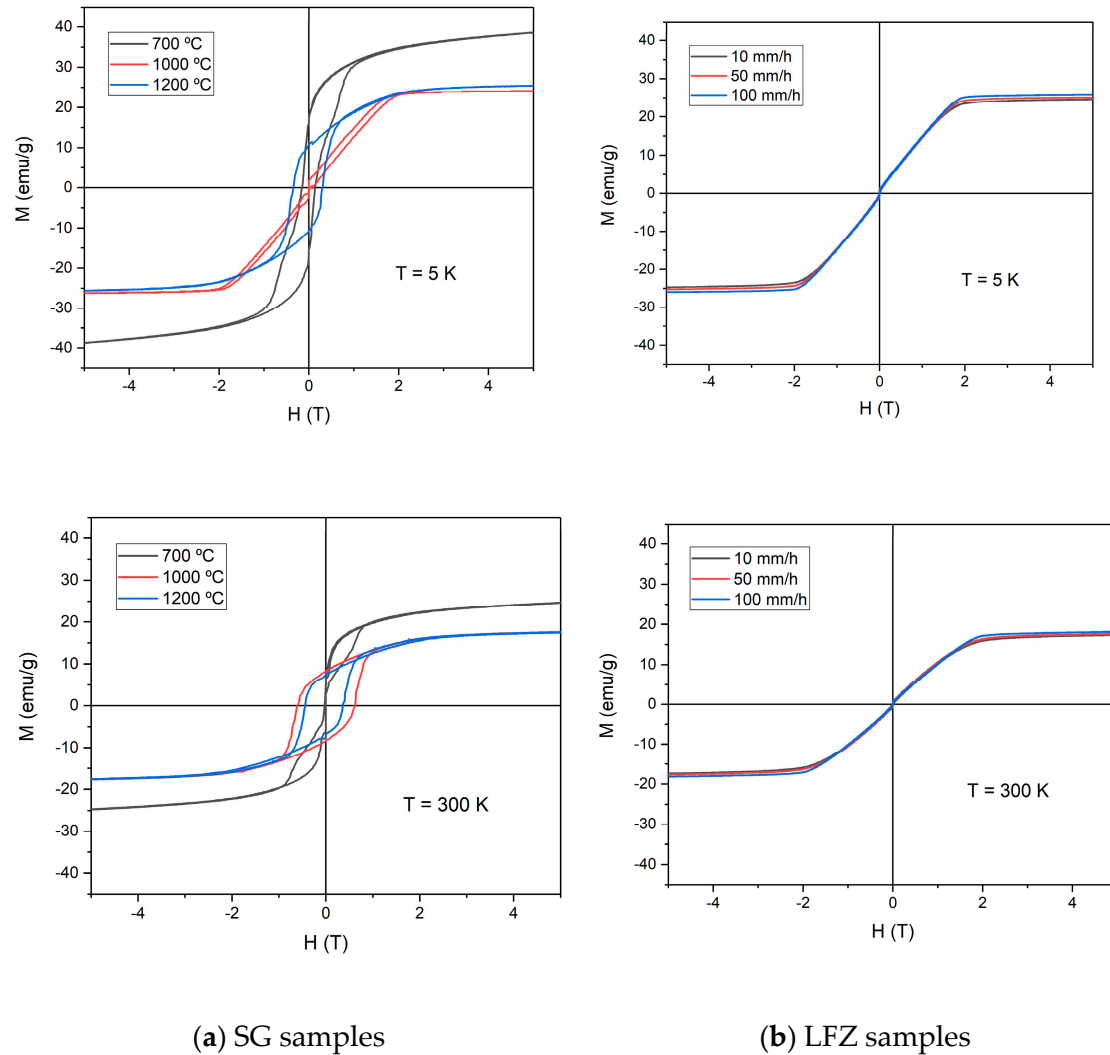

(**a**) SG samples   (**b**) LFZ samples

Figure 8. Hysteresis cycles obtained for 5 K and 300 K for (**a**) SG and (**b**) LFZ samples.

According to the literature [29], it is a common behavior of ferromagnetic materials, for the saturation magnetization decreases with the increase in the temperature of heat treatments. This phenomenon is related to the grain size of the sample, which decreases with increasing temperature [46]. The results obtained are consistent with this trend since the sample treated at 700 °C (smallest grain size, Table 2) is the one with the highest magnetization, while samples treated at 1000 and 1200 °C show similar magnetization. All cycles indicate that all particles have a ferromagnetic behavior, since they have an area in the hysteresis cycle.

From hysteresis cycles obtained for the LFZ samples (Figure 8b), the samples at 5 K have a much higher magnetization than at 300 K (room temperature). All samples seem to tend towards a saturation magnetization that does not change much when comparing

the values of one fiber to another. This can be since they present very similar compositions with the same phases. The fiber grown at 100 mm/h presents the highest magnetization for both temperatures: 25.9 emu/g at 5 K and 18.1 emu/g at 300 K.

Comparing the obtained results (Figure 8), it is possible to conclude that the sample with the highest magnetization is the sample treated at 700 °C, with a value of 38.6 emu/g (T = 5 K). As previously mentioned, magnetization decreases with the increase in the treatment temperature (SG samples), and the same happens with the increase in the pulling rate (LFZ samples). The difference in the behavior of the samples obtained by SG and LFZ is related to the grain's formation in the samples, which varies with the method. In the LFZ samples, the grain boundary density is much lower, and the surface is much less porous, with all samples being very similar. On the other hand, samples obtained by SG have visible differences in grain shape and size when the treatment temperature is increased.

In the sample treated at 700 °C (Figure 9a), the blocking temperature is approximately 287 K, the temperature at which the ZFC and FC lines start to diverge. For the samples treated at 1000 and 1200 °C, it is not possible to determine the blocking temperature since the ZFC lines do not overlap the FC lines in any temperature range analyzed. This fact was due to the analysis method carried out since after the measurement of hysteresis at 300 K, there is a remaining magnetization in the sample, translating into a translation in the measurement under FC relative to ZFC [43].
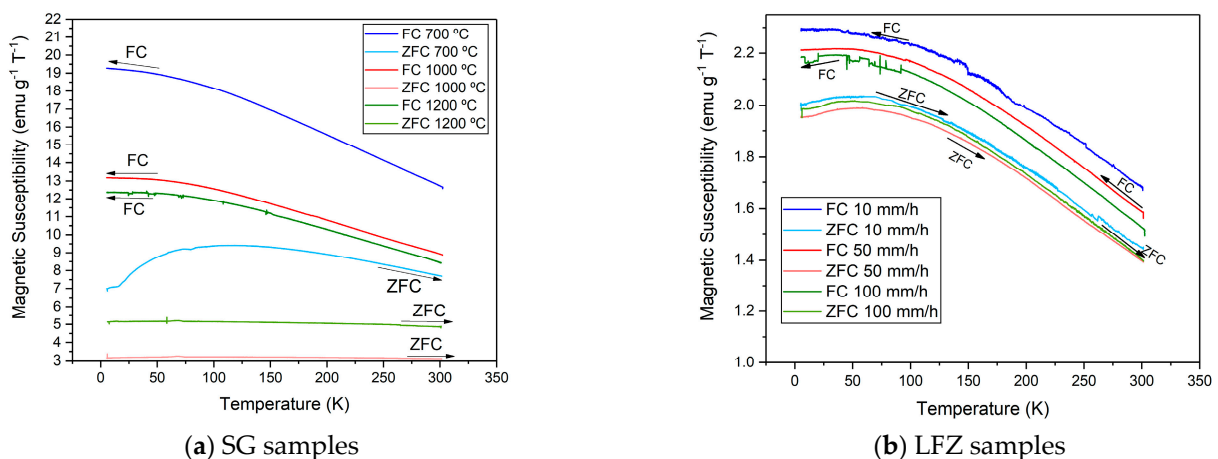

Figure 9. FC and ZFC curves, recorded at 0.1 T, for (**a**) SG samples and (**b**) LFZ samples.

In the samples obtained by LFZ (Figure 9b), the blocking temperature is much easier to define since the divergence of the lines is clear. As previously mentioned, knowledge of the experimental sequence is important, as in these measurements, there is also a translation of the measurement under FZ relative to ZFC, justified by the experimental sequence of magnetic measurements. For samples grown at 10, 50, and 100 mm/h, the blocking temperatures are 66, 50, and 70 K, respectively.

4. Conclusions

The synthesis of strontium ferrite ($SrFe_2O_4$) using two different methods: Sol-Gel via protein, using powdered coconut water as a precursor, and Laser Floating Zone, were studied.

Three treatment temperatures were defined based on thermal analysis for SG samples: 700, 1000, and 1200 °C. For the LFZ, since all samples are obtained by melting, the parameter a to vary was the growth rate of the sample: 10, 50, and 100 mm/h.

In the X-ray diffraction analysis, it was verified that only the sample treated at 700 °C contained a phase of $SrFe_2O_4$. The samples obtained by SG at 1000 and 1200 °C presented the $Sr_4Fe_6O_{13}$ and $SrFe_{12}O_{19}$ phases. These two phases are also present in the samples obtained by LFZ. Raman spectroscopy confirmed the crystalline phases detected in the X-ray analysis.

In the SEM analysis, it was verified that grain size increases with the increase in the treatment temperature between 700 and 1000 °C. Also, the appearance of grains with different shapes and sizes indicates the appearance of new crystalline phases. In the samples obtained by LFZ, a decrease in porosity and crystal growth direction was observed, as well as a change in their length. Through the EDS map, the quantification of the elements on the samples was carried out, making it possible to verify the existence of two phases in the samples.

Regarding the electrical characterization, it was possible to verify the increasing tendency of the DC conductivity with the increase in the treatment temperature of the samples obtained by SG, as well as for the increase in the growth velocity of the samples obtained by LFZ. The sample with the highest DC conductivity was the sample treated at 1200 °C with $\sigma_{dc} = 0.030$ S/m, and the sample with the highest conductivity from the samples obtained by LFZ was the sample grown at 100 mm/h with $\sigma_{dc} = 0.0016$ S/m.

Through impedance spectroscopy, it was concluded that the samples with the highest dielectric constant and lowest losses were the samples treated at 700 °C for 1 kHz: $\varepsilon_r' = 9219$; $\varepsilon_r'' = 75{,}152$; $\tan\delta = 8.1$; $\sigma_{ac} = 0.004$ S/m, for the SG method, and the sample grew at 100 mm/h, for 1 kHz: $\varepsilon_r' = 430{,}712$; $\varepsilon_r'' = 11{,}577$; $\tan\delta = 0.84$; $\sigma_{ac} = 0.0006$ S/m, for the LFZ.

The magnetic analysis allowed to confirm that the samples obtained through the sol-gel method present, in general, greater magnetization than the samples obtained by LFZ. The sample that obtained the highest magnetization was the sample treated at 700 °C with a value of 38.5 emu/g at a temperature of 5 K.

However, when comparing the samples from the two methods, the one with the best relationship between dielectric constant and dielectric losses was the sample obtained by LFZ at 100 mm/h, which is the most suitable for energy storage. The remaining samples presented a high dielectric constant; nevertheless, the dielectric losses were so high that it does not allow energy storage. This indicates that this material can be used in other applications, for example in electromagnetic shielding.

Data Availability Statement: The raw data supporting the conclusions of this article will be made available by the authors on request.

Conflicts of Interest: The authors declare no conflicts of interest.

References

1. Soreto Teixeira, S. *Desenvolvimento de Novos Materiais Para Armazenamento de Energia*; University of Aveiro: Aveiro, Portugal, 2019; Available online: https://hdl.handle.net/10773/30590 (accessed on 2 February 2024).
2. Soreto, S.; Graça, M.; Valente, M.; Costa, L. Lithium Ferrite: Synthesis, Structural Characterization and Electromagnetic Properties. In *Magnetic Spinels—Synthesis, Properties and Applications*; Seehra, M., Ed.; InTech: London, UK, 2017; pp. 31–50.
3. Nguyen, Q.-D.; Choi, C.-G. Recent Advances in Multifunctional Electromagnetic Interference Shielding Materials. *Heliyon* **2024**, *10*, e31118. [CrossRef] [PubMed]
4. Akram, S.; Ashraf, M.; Javid, A.; Abid, H.A.; Ahmad, S.; Nawab, Y.; Rasheed, A.; Xue, Z.; Nosheen, A. Recent Advances in Electromagnetic Interference (EMI) Shielding Textiles: A Comprehensive Review. *Synth. Met.* **2023**, *294*, 117305. [CrossRef]
5. Gingasu, D.; Mindru, I.; Patron, L.; Stoleriu, S. Synthesis of Lithium Ferrites from Polymetallic Carboxylates. *J. Serb. Chem. Soc.* **2008**, *73*, 979–988. [CrossRef]

6. Malaie, K.; Ganjali, M.R. Spinel Nano-Ferrites for Aqueous Supercapacitors; Linking Abundant Resources and Low-Cost Processes for Sustainable Energy Storage. *J. Energy Storage* **2021**, *33*, 102097. [CrossRef]

7. Qin, H.; He, Y.; Xu, P.; Huang, D.; Wang, Z.; Wang, H.; Wang, Z.; Zhao, Y.; Tian, Q.; Wang, C. Spinel Ferrites (MFe_2O_4): Synthesis, Improvement and Catalytic Application in Environment and Energy Field. *Adv. Colloid Interface Sci.* **2021**, *294*, 102486. [CrossRef] [PubMed]

8. Mamatha, C.; Krishnaiah, M.; Prakash, C.S.; Rewatkar, K.G. Structural and Electrical Properties of Aluminium Substituted Nano Calcium Ferrites. *Procedia Mater. Sci.* **2014**, *5*, 780–786. [CrossRef]

9. Majhi, S. *Dielectric and Magnetic Behaviour of Substituted Strontium M-Hexagonal Ferrite*; National Institute of Technology Roukela: Roukela, India, 2012; Available online: https://ethesis.nitrkl.ac.in/4871/ (accessed on 2 February 2024).

10. Dehghani Dastjerdi, O.; Shokrollahi, H.; Mirshekari, S. A Review of Synthesis, Characterization, and Magnetic Properties of Soft Spinel Ferrites. *Inorg. Chem. Commun.* **2023**, *153*, 110797. [CrossRef]

11. Teixeira, S.S.; Amaral, F.; Graça, M.P.F.; Costa, L.C. Comparison of Lithium Ferrite Powders Prepared by Sol-Gel and Solid State Reaction Methods. *Mater. Sci. Eng. B* **2020**, *255*, 114529. [CrossRef]

12. Costa, L.C.; Teixeira, S.S.; Graça, M. Structural, Morphologic and Dielectric Properties of Sodium Ferrites. *AIP Conf. Proc.* **2019**, *2196*, 020008. [CrossRef]

13. Soreto Teixeira, S.; Sales, A.J.M.; Graça, M.P.F.; Costa, L.C. Yttrium Ferrites with Enhanced Dielectric Properties. *Mater. Sci. Eng. B* **2018**, *232–235*, 41–47. [CrossRef]

14. Azab, A.A.; Mansour, A.M.; Turky, G.M. Structural, Magnetic, and Dielectric Properties of $Sr_4Fe_6O_{13}$ Ferrite Prepared of Small Crystallites. *Sci. Rep.* **2020**, *10*, 4955. [CrossRef]

15. Chauhan, C.; Gupta, T.; Jotania, R. Structural and Dielectric Properties of Strontium Hexaferrite Powder Synthesized in Presence of Crown Flowers Extract. *Int. J. Res.* **2017**, *4*, 870–874. Available online: https://journals.pen2print.org/index.php/ijr/article/viewFile/9313/9000 (accessed on 2 February 2024).

16. Yadav, R.S.; Kuřitka, I.; Vilcakova, J.; Havlica, J.; Masilko, J.; Kalina, L.; Tkacz, J.; Enev, V.; Hajdúchová, M. Structural, Magnetic, Dielectric, and Electrical Properties of $NiFe_2O_4$ Spinel Ferrite Nanoparticles Prepared by Honey-Mediated Sol-Gel Combustion. *J. Phys. Chem. Solids* **2017**, *107*, 150–161. [CrossRef]

17. Guo, J.; Li, J.; Kou, H. Chemical Preparation of Advanced Ceramic Materials. In *Modern Inorganic Synthetic Chemistry*; Elsevier: Amsterdam, The Netherlands, 2011; pp. 429–454.

18. Ghahfarokhi, S.E.M.; Shobegar, E.M. Influence of PH on the Structural, Magnetic and Optical Properties of $SrFe_2O_4$ Nanoparticles. *J. Mater. Res. Technol.* **2020**, *9*, 12177–12186. [CrossRef]

19. Danks, A.E.; Hall, S.R.; Schnepp, Z. The Evolution of 'Sol–Gel' Chemistry as a Technique for Materials Synthesis. *Mater. Horiz.* **2016**, *3*, 91–112. [CrossRef]

20. Costa, F.M.; Ferreira, N.M.; Rasekh, S.; Fernandes, A.J.S.; Torres, M.A.; Madre, M.A.; Diez, J.C.; Sotelo, A. Very Large Superconducting Currents Induced by Growth Tailoring. *Cryst. Growth Des.* **2015**, *15*, 2094–2101. [CrossRef]

21. Ferreira, N. *Materials and Concepts for CO_2 Lean Ironmaking by Pyroelectrolysis*; University of Aveiro: Aveiro, Portugal, 2014; Available online: https://hdl.handle.net/10773/14004 (accessed on 2 February 2024).

22. Teixeira, S.S.; Graça, M.P.F.; Costa, L.C. Dielectric, Morphological and Structural Properties of Lithium Ferrite Powders Prepared by Solid State Method. *J. Non-Cryst. Solids* **2012**, *358*, 1924–1929. [CrossRef]

23. Callister, W.D.; David Rethwisch, J.G. *Materials Science and Engineering—An Introduction*, 9th ed.; Wiley: Hoboken, NJ, USA, 2014.

24. Akhtar, K.; Khan, S.A.; Khan, S.B.; Asiri, A.M. Scanning Electron Microscopy: Principle and Applications in Nanomaterials Characterization. In *Handbook of Materials Characterization*; Springer International Publishing: Cham, Switzerland, 2018; pp. 113–145.

25. Jose Chirayil, C.; Abraham, J.; Kumar Mishra, R.; George, S.C.; Thomas, S. Instrumental Techniques for the Characterization of Nanoparticles. In *Thermal and Rheological Measurement Techniques for Nanomaterials Characterization*; Elsevier: Amsterdam, The Netherlands, 2017; pp. 1–36.

26. Smith, E.; Dent, G. *Modern Raman Spectroscopy—A Practical Approach*; Wiley: Hoboken, NJ, USA, 2004; ISBN 9780471496687.

27. Carvalho, J.P.F.; Vieira, T.; Silva, J.C.; Soares, P.I.P.; Ferreira, N.M.; Amorim, C.O.; Teixeira, S.S.; Graça, M.P.F. Potassium Ferrite for Biomedical Applications. *Materials* **2023**, *16*, 3880. [CrossRef] [PubMed]

28. Teixeira, S.S.; Graça, M.P.F.; Lucas, J.; Valente, M.A.; Soares, P.I.P.; Lança, M.C.; Vieira, T.; Silva, J.C.; Borges, J.P.; Jinga, L.-I.; et al. Nanostructured $LiFe_5O_8$ by a Biogenic Method for Applications from Electronics to Medicine. *Nanomaterials* **2021**, *11*, 193. [CrossRef]

29. Langhof, N.; Seifert, D.; Göbbels, M.; Töpfer, J. Reinvestigation of the Fe-Rich Part of the Pseudo-Binary System $SrO–Fe_2O_3$. *J. Solid State Chem.* **2009**, *182*, 2409–2416. [CrossRef]

30. Ferreira, N.M.; Ferro, M.C.; Valente, M.A.; Frade, J.R.; Costa, F.M.; Kovalevsky, A.V. Unusual Redox Behaviour of the Magnetite/Hematite Core–Shell Structures Processed by the Laser Floating Zone Method. *Dalton Trans.* **2018**, *47*, 5646–5651. [CrossRef] [PubMed]

31. Godara, S.K.; Kaur, M.P.; Kaur, V.; Malhi, P.S.; Singh, M.; Verma, S.; Jasrotia, R.; Ahmed, J.; Tamboli, M.S.; Sood, A.K. Investigation of Microstructural and Magnetic Properties of Ca^{2+} Doped Strontium Hexaferrite Nanoparticles. *J. King Saud Univ. Sci.* **2022**, *34*, 101963. [CrossRef]

32. Mohammed, J.; Sa'adu, I.; Wudil, Y.S.; Carol, T.T.; Hafeez, H.Y.; Elnaggar, A.Y.; Mersal, G.A.M.; Ibrahim, M.M.; El-Bahy, Z.M.; Srivastava, A.K. Cation Distribution and Site Occupancy of Nanoscale Cu^{2+}-Er^{3+} Substituted Strontium Hexaferrites via Raman and Mössbauer Spectroscopy. *J. Mol. Struct.* **2022**, *1262*, 133083. [CrossRef]

33. Song, K.; Lee, Y.; Jo, M.R.; Nam, K.M.; Kang, Y.M. Comprehensive Design of Carbon-Encapsulated Fe_3O_4 Nanocrystals and Their Lithium Storage Properties. *Nanotechnology* **2012**, *23*, 505401. [CrossRef] [PubMed]

34. Biswal, S.; Bhaskaram, D.S.; Govindaraj, G. Role of Graphene Oxide in Modifying Magnetism in α-Fe_2O_3 Nanoparticles: Raman and Magnetization Studies. *Mater. Chem. Phys.* **2021**, *266*, 124531. [CrossRef]

35. Mousavi Ghahfarokhi, S.E.; Shobegar, E.M.; Shoushtari, M.Z. Preparation and Characterization of Spinel $SrFe_2O_4$ Nanoparticles by Method Sol-Gel. *J. Aust. Ceram. Soc.* **2021**, *57*, 1359–1369. [CrossRef]

36. Carvalho, R.G.; Fernandes, A.J.S.; Oliveira, F.J.; Alves, E.; Franco, N.; Louro, C.; Silva, R.F.; Costa, F.M. Single and Polycrystalline Mullite Fibres Grown by Laser Floating Zone Technique. *J. Eur. Ceram. Soc.* **2010**, *30*, 3311–3318. [CrossRef]

37. Ferreira, N.M.; Kovalevsky, A.V.; Costa, F.M.; Frade, J.R.; Gauckler, L. Processing Effects on Properties of (Fe, Mg, Al)$_3O_4$ Spinels as Potential Consumable Anodes for Pyroelectrolysis. *J. Am. Ceram. Soc.* **2016**, *99*, 1889–1893. [CrossRef]

38. Sowjanya, C.; Mandal, R.; Pratihar, S.K. Grain Size Dependent Electrical Conductivity, Chemical Surface Exchange and Bulk Diffusion Coefficient of $La_{0.5}Sr_{0.5}A_{10.2}Fe_{0.8}O_3$-$\delta$. *J. Alloys Compd.* **2020**, *818*, 152831. [CrossRef]

39. Gomes, H.C.; Teixeira, S.S.; Graça, M.P.F. Synthesis of Calcium Ferrite for Energy Storage Applications. *J. Alloys Compd.* **2022**, *921*, 166026. [CrossRef]

40. Ahsan, M.Z.; Islam, M.A.; Khan, F.A. Effects of Sintering Temperature on Ac Conductivity, Permittivity, and Permeability of Manganese Doped Cobalt Ferrite Nanoparticles. *Results Phys.* **2020**, *19*, 103402. [CrossRef]

41. Atif, M.; Hanif Alvi, M.; Ullah, S.; Ur Rehman, A.; Nadeem, M.; Khalid, W.; Ali, Z.; Guo, H. Impact of Strontium Substitution on the Structural, Magnetic, Dielectric and Ferroelectric Properties of $Ba_{1-X}Sr_xFe_{11}Cr_1O_{19}$(x = 0.0–0.8) Hexaferrites. *J. Magn. Magn. Mater.* **2020**, *500*, 166414. [CrossRef]

42. Singh, C.; Nikolic, M.V.; Narang, S.B.; Sombra, A.S.B.; Zhou, D.; Trukhanov, S.; Panina, L.; Singh, J.; Trukhanov, A. Controllable Morphology, Dielectric, Magnetic and Reflection Loss Characteristics of Ferrite/Wax Composites for Low-Loss Applications. *J. Alloys Compd.* **2021**, *888*, 161611. [CrossRef]

43. Mahato, D.K. Ac Conductivity Analysis of Nanocrystallite $MgFe_2O_4$ Ferrite. *Mater. Today Proc.* **2018**, *5*, 9191–9195. [CrossRef]

44. Cao, D.; Li, H.; Pan, L.; Li, J.; Wang, X.; Jing, P.; Cheng, X.; Wang, W.; Wang, J.; Liu, Q. High Saturation Magnetization of γ-Fe_2O_3 Nano-Particles by a Facile One-Step Synthesis Approach. *Sci. Rep.* **2016**, *6*, 32360. [CrossRef] [PubMed]

45. Sam, S.A.; Balan, A.P.; Kaipamangalath, A.; Varma, M.R.; Nair, R.R.; Thomas, S. Nanocomposite Permanent Magnets Based on $SrFe_{12}O_{19}$-Fe_3O_4 Hard-Soft Ferrites. *J. Supercond. Novel Magn.* **2021**, *34*, 3333–3344. [CrossRef]

46. Lin, C.-R.; Chu, Y.-M.; Wang, S.-C. Magnetic Properties of Magnetite Nanoparticles Prepared by Mechanochemical Reaction. *Mater. Lett.* **2006**, *60*, 447–450. [CrossRef]